Li *et al. Respiratory Research* (2025) 26:194
https://doi.org/10.1186/s12931-025-03271-0

Respiratory Research

RESEARCH Open Access

Autophagy and exosome dynamics in Radiation-Induced pulmonary fibrosis: the critical role of TRIB3

Na Li[1,2†], Wenyue Zhao[1†], Jiale Li[1], Dengfeng Zhang[1], Kejun Li[1], Mengmeng Yang[1], Xinran Lu[1], Liqing Du[1*], Chang Xu[1*] and Qiang Liu[1*]

Abstract

Objective Dysregulated autophagy plays a critical role in the pathogenesis of pulmonary fibrosis. The stress protein TRIB3 has been correlated with abnormal autophagy, but its specific contribution to radiation-induced pulmonary fibrosis (RIPF) remains unclear. This study aimed to elucidate the role of TRIB3 in RIPF progression.

Methods We conducted RNA-sequencing of rat RIPF lung tissue to analyze the transcriptomic profile and determine gene expression changes in murine with RIPF. We established mouse models with alveolar epithelial type II cells (AEC II)-specific knockdown or overexpression of TRIB3 to elucidate its role in RIPF progression. We utilized mRFP-GFP-LC3 fluorescent reporter cells, nanoparticle tracking analysis, immunofluorescence and immunoprecipitation assays to uncover the underlying mechanisms.

Results TRIB3 expression was elevated in irradiated AEC II. Silencing TRIB3 in AEC II mitigated RIPF in mice, whereas its overexpression exacerbated the condition. Mechanistically, TRIB3 interacted with the LC3-interacting region (LIR) motif and ubiquitin-associated (UBA) domain of sequestosome 1 (SQSTM1), an autophagic receptor protein, thereby inhibiting autophagic flux in AEC II cell line MLE12. This inhibition increased exosome secretion and facilitated crosstalk between MLE12 cells and fibroblasts, ultimately enhancing the proliferation and extracellular matrix production of lung fibroblasts.

Conclusion TRIB3 in AEC II inhibits autophagic flux by interacting with SQSTM1, thereby increasing exosome secretion, which promotes fibroblast proliferation and extracellular matrix production, contributing to RIPF progression.

Keywords Radiation-induce pulmonary fibrosis, TRIB3, Alveolar epithelial type II cells (AEC II), Autophagic flux, Exosome

†Na Li and Wenyue Zhao contributed equally to this work.

*Correspondence:
Liqing Du
duliqing@irm-cams.ac.cn
Chang Xu
xuchang@irm-cams.ac.cn
Qiang Liu
liuqiang@irm-cams.ac.cn

[1]Tianjin Key Laboratory of Radiation Medicine and Molecular Nuclear Medicine, Institute of Radiation Medicine, State Key Laboratory of Advanced Medical Materials and Devices, Chinese Academy of Medical Sciences and Peking Union Medical College, Tianjin Institutions of Health Science, Tianjin 300192, China
[2]Department of Radiology, The First Affiliated Hospital of Guangzhou Medical University, Guangzhou 510120, China

Introduction

Radiation-induced pulmonary fibrosis (RIPF), occurring in 16–28% of thoracic radiotherapy cases [1], is a late complication characterized by fibroblast activation, excessive ECM deposition, and progressive lung dysfunction [2]. As current therapeutic interventions demonstrate limited efficacy in managing RIPF, emphasizing the need to further understand its pathogenesis and develop new therapeutic strategies.

Autophagy, an evolutionarily conserved intracellular degradation pathway, is essential for maintaining intracellular homeostasis [3] and critically regulates pulmonary fibrosis progression. In idiopathic pulmonary fibrosis (IPF), it modulates fibroblast apoptosis and epithelial senescence [4], while CFTR dysfunction in CF impairs epithelial autophagy [5]. Silica-induced fibrosis is attenuated through autophagy-mediated reduction of epithelial apoptosis [6]. yet excessive macrophage autophagy may worsen silicosis by activating fibroblasts [7]. These dual roles highlight autophagy's therapeutic potential for fibrotic lung diseases [8].

Although RIPF shares similar pathological characteristics with other pulmonary fibrotic conditions, its pathogenesis is distinct [9]. Radiation disrupts autophagic machinery [10, 11], yet the precise role of autophagy in cellular responses to radiation remains unclear and potentially context-dependent. Evidence suggests that the type, extent, and timing of stress are important determinants of cell fate following autophagy induction [12]. Thus, the role of autophagy in the RIPF is still unclear.

Recent studies have identified tribbles homolog 3 (TRIB3) as a stress-responsive pseudokinase that is upregulated in various human diseases and plays complex, cell-type-specific roles in autophagy regulation and pulmonary fibrosis pathogenesis [13–16]. In hepatocytes, TRIB3 inhibits autophagic flux by disrupting SQSTM1/p62-LC3 interaction [17], while in neurons it promotes autophagosome formation through ULK1 activation via mTOR inhibition [18]. In the context of IPF, TRIB3 exhibits differential effects across cell types: it impairs alveolar epithelial cell regeneration [19], promotes profibrotic macrophage activation [20], yet paradoxically suppresses fibroblast activation [21]. A recent study has reported that both TRIB3 and p62 are upregulated in activated fibroblasts and lung tissue of IPF mice [22]. These findings point to TRIB3 as a promising target for IPF. Nevertheless, there are currently no studies reporting on TRIB3 in the context of RIPF.

In this study, we examined TRIB3 expression in fibrotic lung tissue from murine models of RIPF and found that TRIB3 inhibited autophagic flux in AEC II and enhances exosome secretion, thereby facilitating RIPF progression. Our findings elucidate the role of TRIB3 in the pathogenesis of RIPF and will provide a reference for future research into preventive and therapeutic strategies for RIPF.

Materials and methods

Antibodies

All primary antibodies used for immunoblotting, immunoprecipitation and immunostaining analysis in the present study are listed as follows: Anti-TRIB3 (B-2) (sc-390242), anti-SQSTM1 (D-3) (sc-28359) and anti-HA tag (F-7) (sc-7392) from Santa Cruz Biotechnology (Texas, USA); anti-fibronectin antibody (ab45688), and anti-MMP2 antibody (ab37150); α-smooth muscle antibody (A5228) and monoclonal anti-FLAG (F-1804) from Sigma (New Jersey, USA); Anti-prosurfactant protein C (SPC) (3432601) from Millipore (California, USA); SQSTM1 polyclonal antibody (18420-1-AP), HA polyclonal antibody (51064-2-AP), mouse IgG (B900620), rabbit IgG (B900610) and GAPDH monoclonal antibody (60004-1-Ig) from Proteintech (Wuhan, China).

Reagents

Pierce™ IP Lysis Buffer (87787), Pierce™ Protein A/G Magnetic Beads (88803) and SuperSignal™ West Pico PLUS Chemiluminescent Substance (34577) were purchased from ThermoFisher Scientific (Massachusetts, USA). Hydroxychloroquine (HY-W031727) was purchased from MCE (New Jersey, USA). RIPA Lysis Buffer (R0020), Hydroxyproline (HYP) Content Assay Kit (BC0225) and Masson's Trichrome Stain Kit (G1340) were purchased from Solarbio (Beijing, China). Lipofectamine® RNAiMAX Reagent (13788-150) and Lipofectamine™ 3000 Reagent (L3000015) were purchased from Invitrogen (California, USA). BCA quantitative kit (P0010) was purchased from Beyotime Biotechnology (Shanghai, China). EdU cell proliferation assay (C10310-1) was purchased from Ribobio (Guangzhou, China).

Establishment of murine RIPF model

All animal experiments were approved by the Animal Ethical and Welfare Committee of the Institute of Radiation Medicine of Peking Union Medical College (IRM-DWLL-2021132). Animals were housed at the Institute of Radiation Medicine, Chinese Academy of Medical Science and Peking Union Medical College, Tianjin, China. All animals were procured from Beijing Huafukang Biotechnology Incorporated Company [SCXK (Beijing) 2019-0008], and were maintained in a specific pathogen-free environment.

The male rats, aged 4–6 weeks and weighing 180–200 g, were anaesthetized with tribromoethanol. As previously published in our study, unilateral right lung irradiation was delivered using a RS-2000 X-ray irradiator (RAD SOURCE Technologies, USA) at a dose rate of 1.522 Gy/min for a cumulative dose of 17 Gy, RIPF

developed 4 months after irradiation [23]. The rats were euthanized by intraperitoneal injection of an overdose of pentobarbital (150 mg/kg).

The RIPF mouse model was established following optimized parameters derived from prior studies conducted by our institutional collaborators [24]. Specifically, the male mice, aged 4–6 weeks and weighing 21–23 g, were anaesthetized with tribromoethanol and irradiated with 17 Gy of X-rays to the unilateral right lung at a dose rate of 2.7 Gy/min, RIPF developed 6 months after irradiation. The mice were euthanized through decapitation.

All animals were closely monitored for changes in respiration and body weight after irradiation. Pulmonary fibrosis was confirmed by haematoxylin and eosin (H&E) staining and Masson's trichrome staining.

RNA extraction and bioinformatic analysis

Total RNA was extracted from lung tissues of rats using Trizol reagent (Invitrogen, California, USA) according to the manufacturer's protocol. RNA sequencing was performed by Gene Denovo Biotechnology Co., Ltd (Guangzhou, China), and the data have been deposited at the NCBI SRA database with the accession number PRJNA1196531. RNAs differential expression analysis (DEGs) was performed by DESeq2 [25] software between normal and RIPF groups. The transcripts with the parameter of false discovery rate (FDR) below 0.05 and absolute fold change ≥ 2 were considered differentially expressed transcripts. Then the DEGs in all or each profile were subjected to Gene Ontology (GO) [26], Kyoto Encyclopedia of Genes and Genomes (KEGG) pathway enrichment analysis [27] and Gene set enrichment analysis [28].

Cell culture

The MLE12 (ATCC® CRL-2110™) cell line, derived from murine lung epithelial type II cells, was procured from the American Type Culture Collection (ATCC, Virginia, USA). The cells were cultured in Ham's F12 medium (HyClone, Utah, USA) supplemented with 2% fetal bovine serum (FBS) (Gibco, New Zealand), 0.005 mg/mL insulin (M&C Gene, Beijing, China), 0.01 mg/mL transferrin (M&C Gene, Beijing, China), 10 nM β-estradiol (M&C Gene, Beijing, China), and 10 nM hydrocortisone (M&C Gene, Beijing, China). NIH/3T3 cells were purchased from ATCC and cultured in DMEM (HyClone, Utah, USA) supplemented with 10% FBS.

Intratracheal administration

After anesthesia with tribromoethanol, the mouse was fixed on the operating board and the glottis was exposed with curved forceps. A 20G trocar was inserted along the glottis, and the core was pulled out after it was in place. After verifying the catheter's placement, 40 to 80 μL of adeno-associated virus was injected using a nebulizing syringe. Following the injection, the syringe was withdrawn, and the operating board was erected for 5 min to allow the drug to infiltrate into the lower lung by gravity, and finally the cannula was withdrawn. The mice were then placed in bedding and warmed with a lamp to monitor their vital signs, including respiration and heartbeat.

Knockdown or overexpression of TRIB3 in mice

Adeno-associated virus 6 (AAV6) was used to carry mice TRIB3 mRNA or short hairpin RNA (shRNA) against mice TRIB3 mRNA, both under the control of the core promoter of SPC (pulmonary surfactant-associated protein C). These AAV6 viruses were produced by Genechem Biosciences Inc (Shanghai, China). Adult male C57BL/6J mice were intratracheally injected with the AAV6 viruses (1×10^{11} viral particles per mouse). Three weeks later, lung tissues were dissected and isolated to verify the knockdown or overexpression of TRIB3 in AEC II using flow cytometry.

Hydroxyproline content assay

Approximately 0.2 g of lung tissue was weighed, minced and 2 mL of extract was added. After digestion by boiling for 2 ~ 6 h, the mixture was centrifuged at 20,000 g for 20 min and the pH was adjusted to 6 ~ 8 with 10 mol/L NaOH. The volume of distilled water was fixed at 4 mL, and the supernatant was taken to detect the absorbance value at 560 nm according to the determination operation table, and the hydroxyproline content of the tissue was calculated.

Masson's trichrome staining

The right lung lobe samples were fixed in 4% formaldehyde solution, embedded in paraffin and sectioned at 5 mm. Lung sections were dried and fixed at 60 °C, dewaxed and hydrated, stained with lapis lazuli blue, haematoxylin, fuchsin and aniline blue staining solution, and finally dehydrated and sealed. Ten random and non-overlapping lung parenchyma visual fields (10x, 20x magnification) were selected to observe and record the changes in collagen fibers in the lung tissue after irradiation.

EdU proliferation assay

NIH/3T3 cells in logarithmic growth phase were taken, and 50,000 cell per well were seeded into the cell slides of 12-well plates. The next day, they were treated with different conditions, and three days later, according to the EdU cell proliferation assay instructions, EdU labelling, cell fixation and Apollo staining were performed, and finally the number of EdU-positive cells was measured and counted under a microscope.

Transwell migration assay

NIH/3T3 cells were seeded into the upper chamber of a 24-well transwell plate, and DMEM medium with 10% FBS was added to the lower chamber and incubated at 37 °C for 12 h. Non-migrated are wiped off with a cotton swab, and then the cells under the filter are fixed and stained with 0.25% crystal violet. Five random areas are selected and counted to measure the cell migration ability.

Extraction and quantification of exosomes

After MLE12 cells were fused to 40–50%, they were washed with PBS and exosome free serum complete medium was added. After 72 h of cell culture, the culture supernatant was collected and the exosome precipitate was obtained by differential centrifugation. 10 μL of exosome suspension was taken out and added to RIPA lysis buffer, the temperature was set at 4℃ and the lysis time was set at 30 min. After lysis, the protein content in the exosomes was quantified using the BCA quantitative kit, and then the exosomes were calculated from the protein standard curve. Nanoparticle tracking analysis (NTA) is the other method used to measure nanoparticle number concentrations in this experiment. Nanoparticles in the isolated exosome suspensions were analyzed using the ZetaView® instrument (Particle Metrix, Meerbusch, Germany). Analysis settings were optimized and kept constant between samples, all experiments were performed at 1:1000 dilution, particle concentrations in the range of 1×10^8/ml particles according to the manufacturer's recommendations. All samples were analyzed in triplicate.

SiRNA knockdown

The siRNAs were synthesized by GenePharma Co., Ltd (Shanghai, China). The nonsense siRNA control and siRNA against TRIB3 (sense 5′- GUCGCUUUGUCUU CAGCAATT-3′; antisense 5′- UUGCUGAAGACAAA GCGACTT-3′) were transfected into MLE12 cell with Lipofectamine RNAiMAX (13778075, ThermoFisher Scientific, Massachusetts, USA). Cells were collected at different times for analysis.

Western blot

Cell extracts were lysed with RIPA lysis buffer (150 mmol/L NaCl, 50 mmol/L Tris, pH = 8.0, 1% Triton X-100, 0.5% sodium deoxycholate, 0.1% SDS, plus protease and phosphatase inhibitors). After the lysis is complete, the protein concentration was quantified with the BCA quantitative kit. Protein was separated in bromophenol blue using sodium dodecyl sulfate-polyacrylamide gel electrophoresis, transferred to the polyvinylidene fluoride membrane, blocked with 1% bovine serum albumin, then incubated with diluted primary antibodies and secondary antibodies, and finally the protein signal was detected in the gel imager using ECL chemiluminescence detection kit.

Measurement of autophagic flux

Autophagic flux was traced with expression of mRFP-GFP-LC3 fusion protein in MLE12 cells. Briefly, we generated a MLE12 cell line that stably expresses mRFP-GFP-LC3 fusion protein by lentiviral transduction. The cells were then transfected with TRIB3 siRNA or TRIB3 overexpression plasmid. Subsequently, the cells were exposed to an 8 Gy dose of irradiation 24 h post-transfection. Autophagic flux was analyzed by fluorescence microscopy monitoring the distribution and alteration of mRFP-GFP-LC3B fluorescent signals at 48 h post-irradiation. The ratio of green to red fluorescence was quantified by high content cell imaging (Molecular Devices, Shanghai, China).

Co-Immunoprecipitation

Protein A/G magnetic beads were washed three times with the appropriate amount of lysis buffer, and 2 μg of the corresponding antibody was added and incubated slowly for 2 h at room temperature to couple the antibody with protein A/G magnetic beads. Cells were collected 48 h after transfection, 1 mL of cell lysis buffer (containing protease inhibitor) was added and the cells were lysed on ice for 30 min, and the cell lysate was centrifuged at 4 °C for 15 min at 12,000 rpm and the supernatant was collected. 60 μL of lysates was added to 4×SDS loading buffer, boiled for 10 min at 100 °C for Western blot analysis, and the remaining lysates was added to the pretreated antibody-magnetic bead mixture and incubated slowly overnight at 4 °C with. After the immunoprecipitation reaction, the magnetic beads were adsorbed to the side of the tube by the magnetic holder. The supernatant was carefully aspirated, and the magnetic beads were washed three times with 1 ml washing buffer. Finally, 100 μL of 2×SDS loading buffer was added, boiled for 10 min at 100 °C, and the interacting proteins were detected by Western blotting.

Statistical analysis

Statistical analysis between groups was performed by SPSS 15.0 software. Enumeration data were analyzed by unpaired t-test. Measurement data were analyzed either by Student's t-test or one-way analysis of variance (ANOVA). $p < 0.05$ was considered statistically significant ($^{*}P < 0.05$, $^{**}P < 0.01$, $^{***}P < 0.001$, ns: no significance). Each experiment was replicated at least three times. The results of the control group and each experimental group were taken as the mean of three different experimental samples and expressed as the mean ± S.E.M.

Results

Changes in the transcriptional profiles of RIPF rats

To investigate the gene expression changes associated with RIPF in murine, we conducted RNA sequencing and transcriptomic analysis on lung tissues from RIPF and normal rats. The resultant RNA-sequencing data have been archived in the NCBI Sequence Read Archive (SRA) database under the accession number PRJNA1196531 [29].

Differentially expressed genes (DEGs) were identified based on the threshold of adjusted $P<0.001$ and fold change (FC) >2 or <0.5, yielding 610 DEGs: 374 genes upregulated and 236 genes downregulated in the RIPF group compared to the normal group (Fig. 1A). The cluster heatmap displayed all DEGs between the two groups (Fig. 1B).

Gene Ontology (GO) enrichment analysis indicated that DEGs were predominantly associated with cell surface, membrane part, extracellular region part, and membrane biological processes (Fig. 1C), suggesting disruptions in intercellular signaling and membrane structures, such as vesicles, in the RIPF group. Kyoto Encyclopedia of Genes and Genomes (KEGG) pathway analysis further highlighted phagosome as the most significantly enriched pathway (Fig. 1D). Gene set enrichment analysis (GSEA) confirmed the enrichment of both phagosome and lysosome pathways in RIPF tissues compared to controls (Fig. 1E, F), implicating altered expression of genes regulating phagocytosis in the lung tissue of RIPF rat.

Elevated TRIB3 expression in murine models of RIPF

Given the growing body of evidence for the role of TRIB3 in IPF and its association with phagosome/ lysosome function [30, 31], we utilized our RNA-sequencing data to explore the correlation between TRIB3 and genes implicated in fibrosis. Our analysis revealed a strong positive correlation between TRIB3 and fibrosis-related genes, including vimentin, TIMP2, MMP12, and FN1 (Figure S1). While initial transcriptomic data suggested a trend towards elevated TRIB3 expression, this did not reach statistical significance (Fig. 2A). However, further analysis using RT-PCR on lung tissue samples from RIPF rats demonstrated a significant upregulation of TRIB3 mRNA (Fig. 2B), a finding corroborated in RIPF mice (Fig. 2C). To substantiate these findings, we assessed TRIB3 protein expression in murine models of RIPF using Western blotting. The results indicated a substantial increase in TRIB3 protein levels in both RIPF rats (Fig. 2D) and mice (Fig. 2E) compared to control groups. However, mouse RIPF lung tissue showed more individual variability. Immunohistochemical staining of lung sections from rats and mice further confirmed these results, showing a pronounced increase in TRIB3 expression in radiation-injured tissues of RIPF models relative to controls (Fig. 2F, G), underscoring the potential role of TRIB3 in the pathogenesis of RIPF.

To investigate the cellular localization of TRIB3 in lung tissue, we analyzed the public single-cell RNA-sequencing dataset GSE211713, which comprises 20 mouse lung samples collected 1 to 5 months after radiation injury. Our single-cell analysis revealed that TRIB3 was predominantly enriched in pulmonary AEC II clusters (Fig. 2H). Given the critical role of AEC II in pulmonary fibrosis [9], we used surfactant protein C (SPC), a hydrophobic protein specific to AEC II, as a marker. Co-staining of mouse lung sections for TRIB3 and SPC confirmed elevated TRIB3 expression specifically within AEC II in RIPF regions (Fig. 2I). Consistently, immunofluorescence staining of rat tissue sections also showed increased TRIB3 protein expression in AEC II after IR injury (Figure S2). Furthermore, flow cytometric analysis of enzymatically digested lung tissue provided additional evidence for the increased co-expression of TRIB3 and SPC in RIPF (Fig. 2J). In vitro, MLE12 cells (a murine AEC II cell line) exposed to a single 8 Gy dose of X-ray irradiation exhibited increased TRIB3 protein levels (Fig. 2K). Collectively, these results indicate that TRIB3 expression is upregulated in IR-injured AEC II in RIPF models.

Silencing TRIB3 in AEC II alleviates RIPF in mice

To investigate the role of TRIB3 in RIPF, we tested three TRIB3-specific short hairpin RNAs (shRNAs) delivered by lentivirus in MLE12 cells, and the TRIB3 depletion level was confirmed by western blotting (Figure S3). Given TRIB3 mainly enriched in AEC II, to further examine TRIB3's role in RIPF, we generated AEC II-specific TRIB3 knockdown mice using an AAV6-SPC-shTRIB3 vector delivered via intratracheal (IT) injection (Fig. 3A). IT delivery of AAV6 vector has been shown to mediate efficient transduction of epithelial cells in mouse lungs [32, 33], also as evidenced by immunofluorescent staining of lung sections (Figure S4). This vector delivers TRIB3 shRNA under the control of the alveolar-specific SPC promoter, specifically knocking down TRIB3 in mouse AEC II. Three weeks after infection, flow cytometry confirmed reduced TRIB3 expression in AEC II of AAV6-SPC-shTRIB3 mice (Fig. 3B). Then, the right lungs of mice were exposed to a single dose of 17 Gy X-ray irradiation. Six months after irradiation, the mice were euthanized and lung tissues were collected. Western blotting showed the TRIB3 protein levels increased markedly after IR, and AAV6-SPC-shTRIB3 mice exhibited significantly lower TRIB3 protein levels compared to AAV6-SPC-shNC mice (Fig. 3C). The differences between AAV6-SPC-shNC and AAV6-SPC-shTRIB3 groups without IR are marginal, which may be due to the low expression level

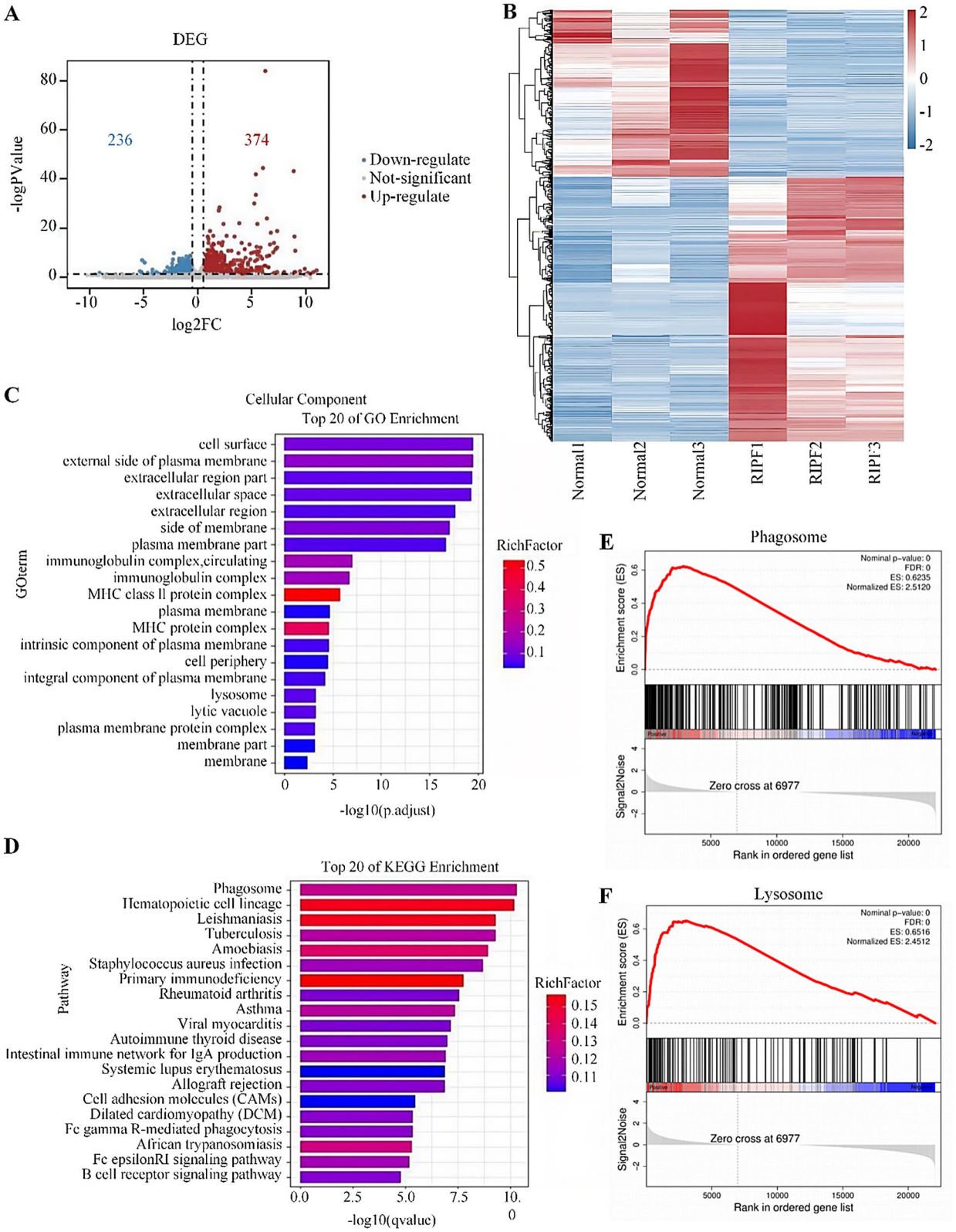

Fig. 1 Transcriptome analysis of RIPF rat lungs. **(A)** Volcano plot of DEGs between groups in transcriptome. **(B)** Heatmap of DEG clustering. **(C)** GO enrichment analysis for cellular components. **(D)** KEGG pathway enrichment analysis. **(E, F)** GSEA for phagosome pathway **(E)** and lysosome pathway **(F)**

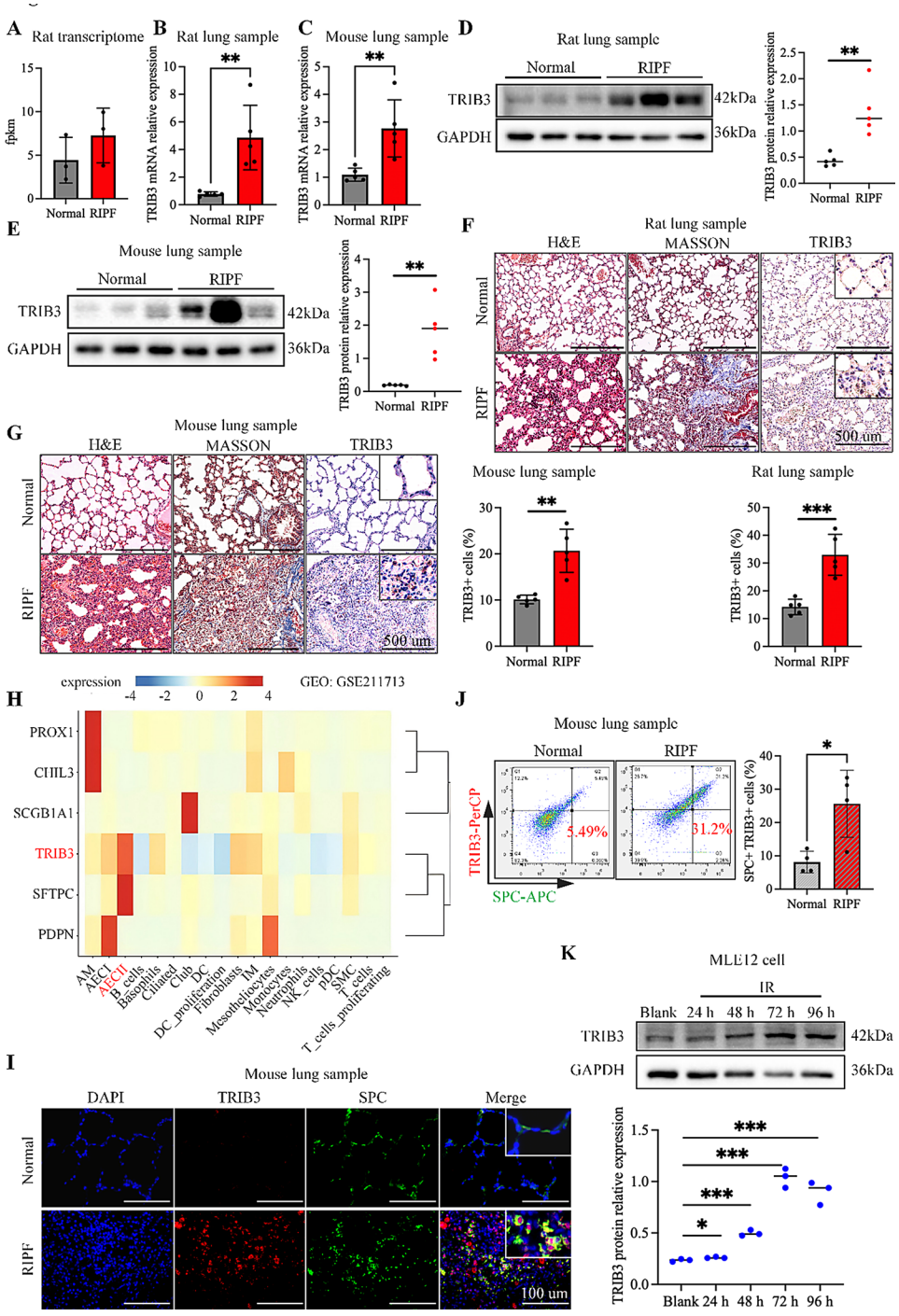

Fig. 2 Increased TRIB3 expression in AEC II of RIPF models. **(A)** TRIB3 mRNA expression in the lung transcriptome of RIPF rats. **(B)** RT-PCR analysis of TRIB3 mRNA in the lung of RIPF rats. **(C)** RT-PCR analysis of TRIB3 mRNA in the lung of RIPF mice. **(D)** Western blot and quantitative analysis of TRIB3 protein in rat lung tissues. ($n = 5$). **(E)** Western blot and quantitative analysis of TRIB3 protein in mouse lung tissues. ($n = 5$). **(F)** Representative images of H&E and Masson staining of rat lung tissue 4 months after irradiation, along with immunohistochemical staining images for TRIB3 and quantitative analysis. The black boxes indicate areas shown at 40× magnification in each micrograph. (Bar = 500 μm; $n = 5$). **(G)** Representative images of H&E and Masson staining of mouse lung tissue 6 months after irradiation, along with immunohistochemical staining images for TRIB3 and quantitative analysis. The black boxes indicate areas shown at 40× magnification in each micrograph. (Bar = 500 μm; $n = 5$). **(H)** Single-cell RNA sequencing heatmap of TRIB3 expression in RIPF mouse lung. **(I)** Representative immunofluorescence images of lung sections from normal and RIPF mice stained with anti-TRIB3 (red), anti-SPC (green), and DAPI (blue). ($n = 5$). Bar = 200 μm. The white boxes in the upper right indicate areas shown at 40× magnification. **(J)** Flow cytometric analysis of co-staining for TRIB3 and SPC in enzymatically digested mouse lung samples and quantitative analysis indicates the percentage of cells co-expressing TRIB3 and SPC. **(K)** Western blot and quantitative analysis of TRIB3 expression in MLE12 cells. (Blank: MLE12 cell without IR). All data are presented as mean ± S.E.M, $^{***}P < 0.001$, $^{**}P < 0.01$, $^{*}P < 0.05$

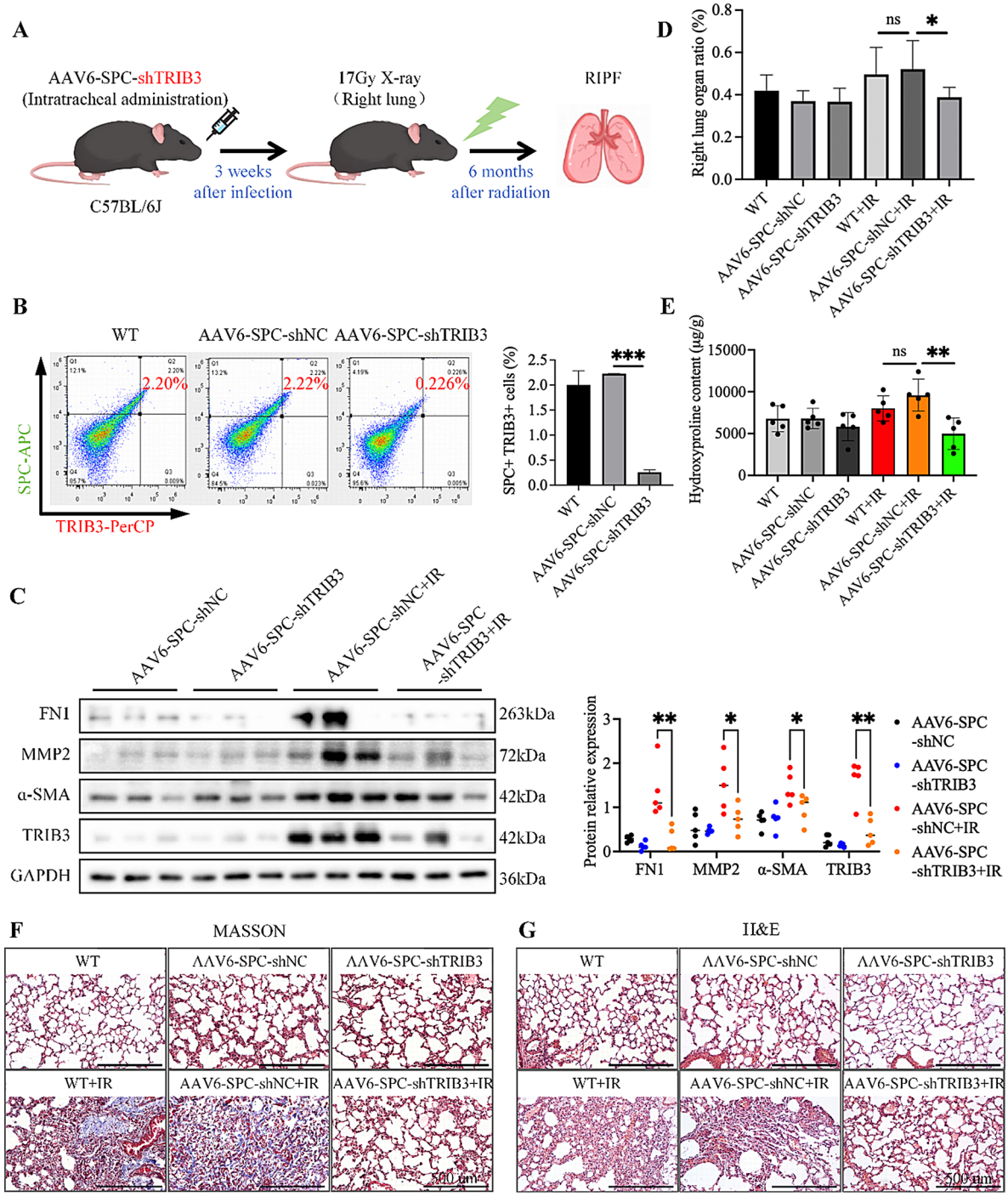

Fig. 3 Silencing TRIB3 in AEC II alleviates RIPF in mice. **(A)** Schematic illustration of experimental design. **(B)** Flow cytometry image and quantitative analysis of TRIB3 + SPC + AEC II isolated from lung samples of mice three weeks after IT administration with AAV6-SPC-shNC or AAV6-SPC-shTRIB3. **(C)** Western blot and quantitative analysis of TRIB3, FN1, MMP2, and α-SMA protein expression in the lungs of indicated mice. GAPDH was used as a loading control. **(D)** Quantitative analysis of the ratio of right lung weight to body weight. **(E)** Hydroxyproline contents in lung tissues. **(F)** Representative Masson staining image of the lung tissues. (Bar = 500 μm). **(G)** Representative H&E staining image of the lung tissues. (Bar = 500 μm). All data are presented as mean ± S.E.M, ***$P < 0.001$, **$P < 0.01$, *$P < 0.05$, ns: no significance

of TRIB3 in normal mice. The AAV6-SPC-shTRIB3 mice also exhibited reduced right lung weight-to-body weight ratios (Fig. 3D), lower hydroxyproline content (Fig. 3E), and decreased collagen deposition as indicated by Masson staining (Fig. 3F). Histological analysis showed that TRIB3 silencing significantly alleviated extracellular matrix hyperplasia and architectural disruption in RIPF lungs (Fig. 3G). Additionally, TRIB3 knockdown reduced

extracellular matrix protein levels (FN1, MMP2, and α-SMA) (Fig. 3C). These findings suggest that AEC II-specific TRIB3 silencing mitigates RIPF in mice.

Overexpression of TRIB3 in AEC II exacerbates RIPF in mice

To evaluate TRIB3 overexpression's effect on RIPF, AEC II-specific TRIB3 overexpression was achieved using an AAV6 serotype vector expressing TRIB3 delivered via IT injection (AAV6-SPC-TRIB3 mice) (Fig. 4A). Six months post- irradiation, AAV6-SPC-TRIB3 mice exhibited increased hydroxyproline content in lung tissues (Fig. 4B), greater collagen deposition (Fig. 4C), and more severe architectural damage as observed by H&E staining (Fig. 4D), along with increased extracellular matrix protein levels (FN1, MMP2) (Fig. 4E). These results indicate that TRIB3 overexpression in AEC II exacerbates RIPF in mice.

TRIB3 promotes crosstalk between MLE12 and fibroblasts via increased exosome secretion

Activated fibroblasts exhibit an enhanced ability to proliferate and synthesize ECM, contributing significantly to the deformation of lung tissue and the development of fibrosis [34]. Notably, the fibronectin 1 (FN1) in the ECM is preferentially expressed and plays a crucial role in the activation of myofibroblasts [35]. To examine whether

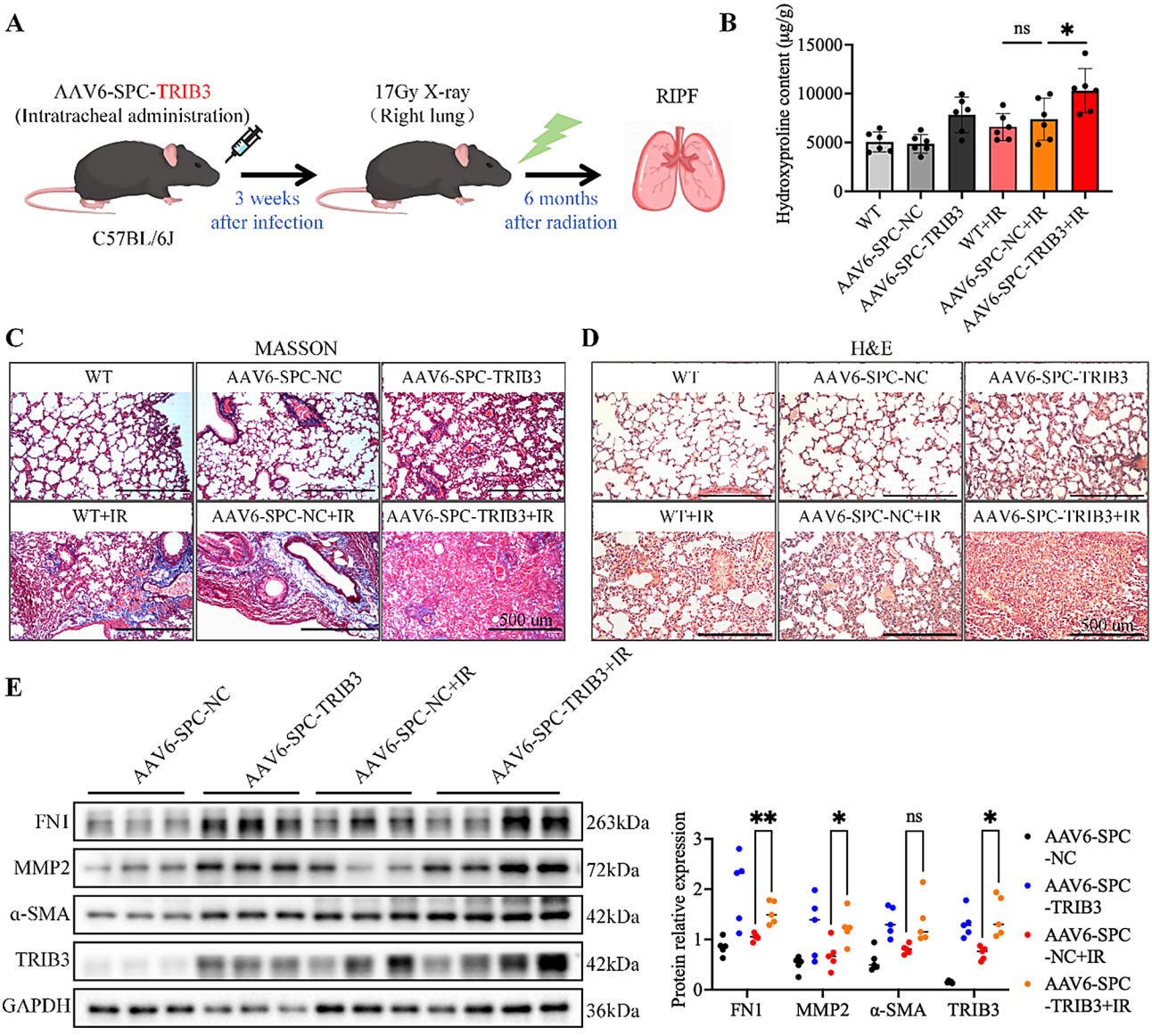

Fig. 4 TRIB3 overexpression in AEC II aggravates RIPF in mice. **(A)** Schematic illustration of experimental design. **(B)** Hydroxyproline contents in the lungs. **(C)** Representative Masson staining image of the lung tissues. (Bar = 500 μm). **(D)** Representative H&E staining image of the lung tissues. (Bar = 500 μm). **(E)** Western blot and quantitative analysis of TRIB3, FN1, MMP2, and α-SMA protein levels in the lungs of mice. Data represent three of five results. All data are presented as mean ± S.E.M, ***$P < 0.001$, **$P < 0.01$, *$P < 0.05$, ns: no significance

AEC II with elevated TRIB3 expression affect fibroblasts, we used a lentiviral vector to overexpress TRIB3 in MLE12 cells (LV-TRIB3 MLE12), whose conditioned media (CM) led to increased FN1 expression (Fig. 5B), proliferation (Fig. 5C, E) and migration (Fig. 5D, F) of murine fibroblasts (NIH/3T3). Given the role of hypoxia-induced exosomes from alveolar epithelial cells in fibroblast activation [36], we speculated that TRIB3 overexpression in MLE12 cells might affect lung fibroblasts via exosomes. To address it, we first performed transcriptomic correlation analysis of TRIB3 and exosome-related genes in RIPF and normal rat lungs. As shown in Fig. 5G, the exosome-related genes TSG101, CD9, CD63 showed a significant positive correlation with TRIB3 expression. We then depleted exosomes from LV-TRIB3 MLE12 CM and found that the effect of CM on FN1 expression in fibroblasts disappeared (Fig. 5H), implying the critical role of exosomes in CM. Subsequently, we isolated exosomes from LV-NC and LV-TRIB3 MLE12 CM by differential centrifugation. Interestingly, when fibroblasts were incubated with a controlled amount (40 μg) of exosomes from LV-NC or LV-TRIB3 MLE12 cells, FN1 expression remained unchanged (Fig. 5I), suggesting that TRIB3 may promote exosome secretion from MLE12 cells. Nanoparticle tracking analysis and immunofluorescence staining for the exosome marker CD81 confirmed increased exosome secretion from LV-TRIB3 MLE12 cells compared to LV-NC MLE12 cells (Fig. 5J, K). Furthermore, exosomes promoted NIH/3T3 fibroblast proliferation and FN1 expression in an exosome concentration-dependent manner (Fig. 5L, M). These results suggest that TRIB3 may argument exosome secretion of MLE12 cell, thereby promoting MLE12-NIH/3T3 crosstalk.

TRIB3 inhibits autophagic flux to augment exosome secretion from AEC II

Inhibition of autophagic flux is a known factor influencing exosome secretion [37]. Gene set variation analysis (GSVA) of the RIPF rat lung transcriptome revealed enrichment of several genes associated with autophagy (Fig. 6A). Notably, TRIB3 exhibited a significant correlation with autophagy-associated genes such as LAMP1, LAMP2, and SQSTM1 (Fig. 6B). Emerging evidence suggests that autophagic flux is inhibited in the lung tissues of IPF, as manifested by a decline in autophagosomes, impaired fusion with lysosomes, and elevated levels of intracellular SQSTM1, particularly insoluble SQSTM1 protein [38–40]. Compared to normal lung tissues, the aggregation of insoluble SQSTM1 was increased in fibrotic lung tissues (Fig. 6C), suggesting impaired autophagic flux in RIPF. Elevated SQSTM1 levels in fibrotic lung tissues were confirmed by immunohistochemical staining (Fig. 6D, E) and co-staining with SPC in AEC II (Fig. 6F). Similar findings were observed in the lungs of RIPF rats (Figure S5). To further investigate the impact of TRIB3 on autophagic activity in RIPF, we examined AAV6-SPC-TRIB3 and AAV6-SPC-shTRIB3 mice. TRIB3 overexpression led to increased aggregation of SQSTM1 in RIPF lung tissue (Fig. 6G, I), while TRIB3 silencing reduced SQSTM1 aggregation (Fig. 6H, J). These results indicate an inverse correlation between TRIB3 expression and autophagic flux in RIPF.

Following exposure to different doses of irradiation, the expression of SQSTM1 and insoluble SQSTM1 were found to be upregulated in MLE12 cells (Fig. 7A). In irradiated MLE12 cells, TRIB3 knockdown decreased insoluble SQSTM1 accumulation, whereas TRIB3 overexpression led to increased accumulation of insoluble SQSTM1 (Fig. 7B, C). The fusion of autophagosome with lysosomes is a crucial step in autophagic flux [41]. To assess whether TRIB3 inhibits this fusion process, we expressed tandem fluorescent-tagged LC3 (mRFP-GFP-LC3) in MLE12 cells to trace the formation and degradation of autophagosomes and autolysosomes [42]. GFP fluorescence is quenched in the acidic environment of lysosomes, while mRFP fluorescence, being less pH-sensitive, remains within the acidic lysosome. A higher GFP/mRFP signal ratio indicates more autophagosomes (green) before fusion with lysosomes, suggesting a blockage of autophagic flux. In contrast, a lower GFP/mRFP signal ratio indicates more mRFP-GFP-LC3 localized to autolysosomes (red), suggesting autophagic flux is occurring. Autophagic flux analysis using mRFP-GFP-LC3 revealed that TRIB3 silencing decreased the GFP/mRFP fluorescence ratio, indicating more autolysosome formation (Fig. 7D). Conversely, TRIB3 overexpression had the opposite effect, suggesting blockage of autophagic flux (Fig. 7E). The lysosomal marker LAMP2 was reduced in TRIB3-overexpressing MLE12 cells (Fig. 7F), implying less autolysosome formation. Together, these findings confirm that TRIB3 inhibits autophagic flux in irradiated MLE12 cells.

To examine whether TRIB3-induced exosome secretion results from autophagic flux inhibition, we treated LV-shTRIB3 MLE12 cells with hydroxychloroquine (HCQ) to block autophagosome-lysosome fusion. HCQ treatment increased exosome secretion in LV-shTRIB3 MLE12 cells post-irradiation (Fig. 7G), suggesting that TRIB3 augments exosome secretion by inhibiting autophagic flux.

TRIB3 interacts with autophagic receptor protein SQSTM1

TRIB3 interacts with SQSTM1 to inhibit autophagic flux in hepatocytes [17]. To determine if this interaction also occurs in RIPF mice, we co-stained TRIB3 and SQSTM1 in lung tissues of AAV6-SPC-NC and AAV6-SPC-TRIB3 RIPF mice. We observed TRIB3 and SQSTM1 co-localization in murine lung tissue (Fig. 8A). Furthermore,

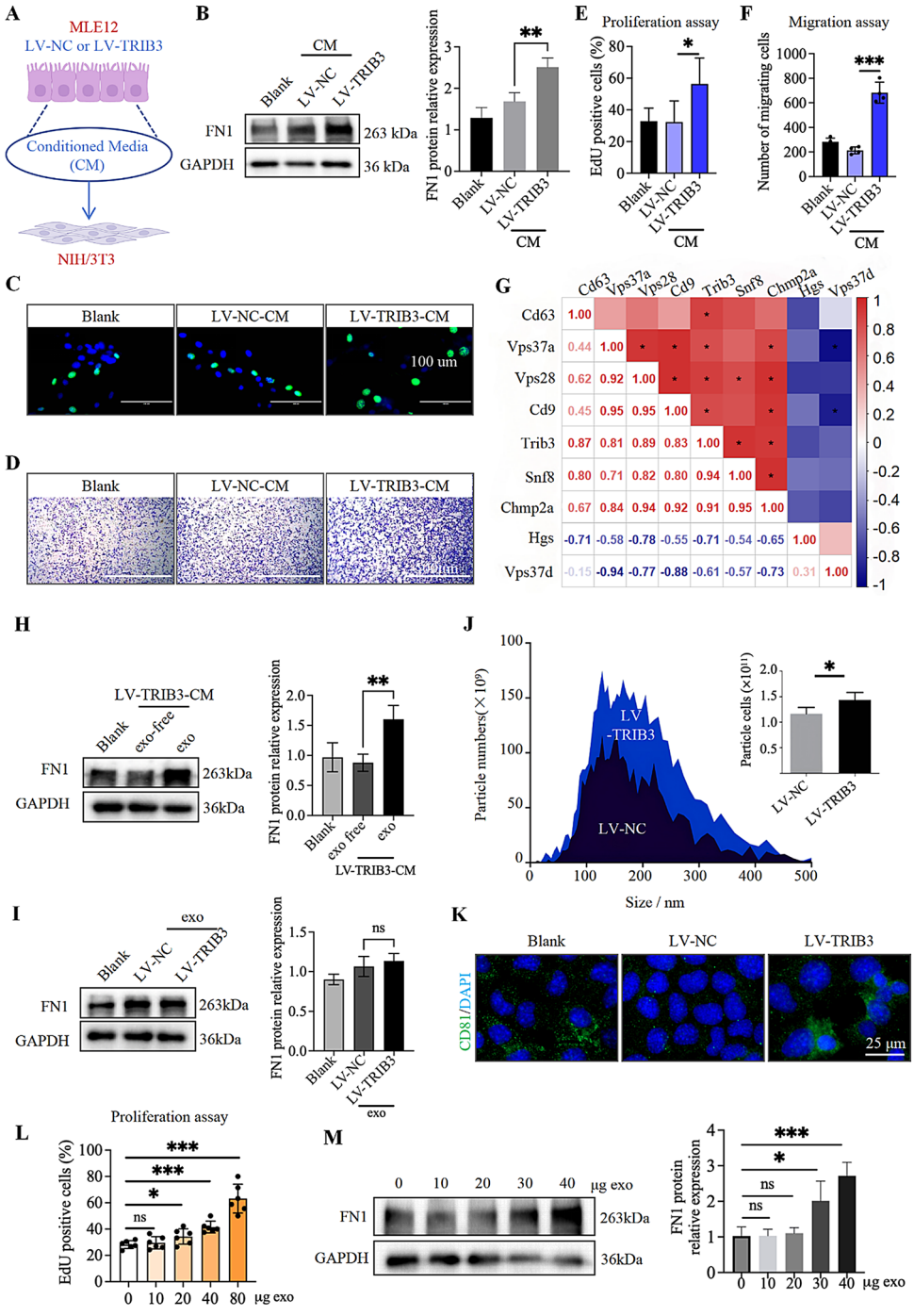

Fig. 5 TRIB3 promotes crosstalk between MLE12 Cells and fibroblasts by increasing exosome secretion. **(A)** NIH/3T3 fibroblasts were incubated in conditioned media (CM) from MLE12 cells. **(B)** Western blot and quantitative analysis of FN1 expression in NIH/3T3 cells incubated with CM from LV-NC or LV-TRIB3 MLE12 cells. Representative EdU assay image **(C)** and quantitative analysis **(E)** of fibroblast proliferation after incubation with indicated CM for 72 h. (Bar = 100 μm). Representative transwell assay image **(D)** and quantitative analysis **(F)** of fibroblast migration after incubation with indicated CM. (Bar = 500 μm). **(G)** Heatmap of the transcriptomic correlation analysis of TRIB3 and exosome-related genes in RIPF and normal rat lung. **(H, I)** Western blot and quantitative analysis of FN1 expression in NIH/3T3 cells after incubation with CM for 72 h. (Blank: DMEM medium with 10% FBS; LV-TRIB3-CM exo-free: CM from LV-TRIB3 MLE12 cells without exosomes; LV-TRIB3 CM: CM from LV-TRIB3 MLE12 cells with exosomes; LV-NC exo: 40 μg exosomes from CM of LV-NC MLE12 cells; LV-TRIB3 exo: 40 μg exosomes from LV-TRIB3 MLE12 cells). **(J)** Exosome quantities from LV-NC and LV-TRIB3 MLE12 cells detected by Nanoparticle Tracking Analysis (NTA). **(K)** Immunofluorescent staining of CD81 (exosome marker) in LV-NC and LV-TRIB3 MLE12 cells. (Bar = 25 μm). **(L)** Quantitative analysis of EdU assays showing the proliferation of NIH/3T3 cells after exposure to indicated amounts of exosomes from MLE12 cells for 72 h. **(M)** Western blot and quantitative analysis of FN1 expression in NIH/3T3 cells after exposure to different concentrations of exosomes from MLE12 cells for 72 h. All data are presented as mean ± S.E.M, ***$P < 0.001$, **$P < 0.01$, *$P < 0.05$

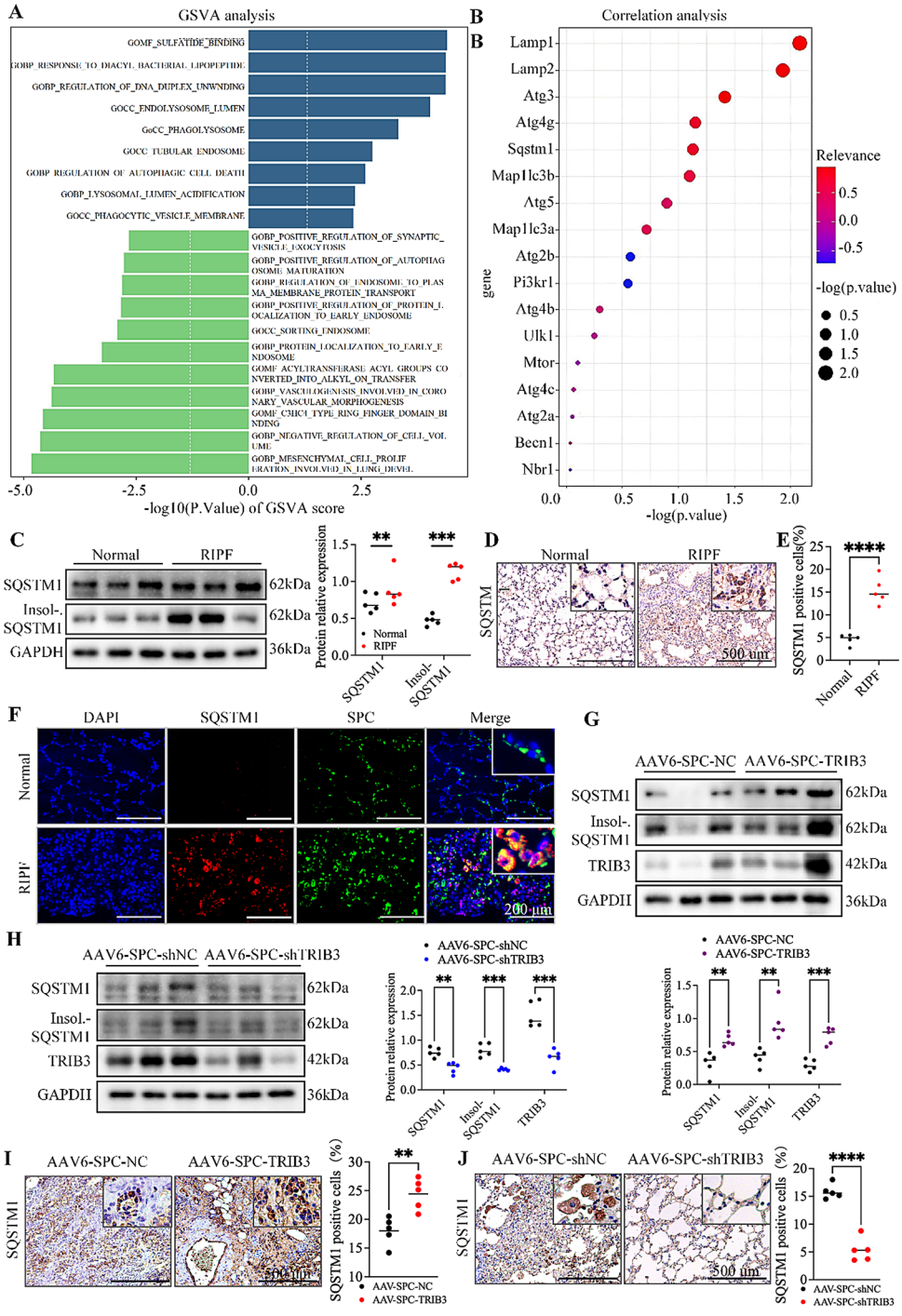

Fig. 6 TRIB3 inhibits autophagic flux in RIPF mice. **(A)** Gene set variation analysis (GSVA) of RIPF rat lung transcriptome. **(B)** Transcriptomic correlation analysis of TRIB3 and autophagy-related genes in RIPF and normal mice. **(C)** Western blot and quantitative analysis of SQSTM1 and insoluble SQSTM1 protein in lung tissues of mice. Data represent results from five animals per group. **(D, E)** Immunohistochemical staining and quantitative analysis of SQSTM1 in mouse lung tissue. Black boxes indicate areas shown at 40× magnification. (Bar = 500 μm; $n = 5$). **(F)** Immunofluorescent staining and quantitative analysis of SQSTM1 (red) in AEC II (SPC, green; DAPI, blue) in lung tissues of mice. White boxes indicate areas shown at 40× magnification. (Bar = 200 μm). **(G, H)** Western blot and quantitative analysis of TRIB3, SQSTM1, and insoluble SQSTM1 in lung tissues of AAV6-SPC-NC or AAV6-SPC-TRIB3 mice **(G)** and AAV6-SPC-shNC or AAV6-SPC-shTRIB3 mice **(H)**. Data represent results from five mice per group. **(I, J)** Immunohistochemical staining and quantitative analysis of SQSTM1 in lung tissues of TRIB3 overexpression RIPF mice **(I)** and TRIB3 knockdown RIPF mice **(J)**. Black boxes indicate areas shown at 40× magnification. (Bar = 500 μm; $n = 5$). All data are presented as mean ± S.E.M, $^{***}P < 0.001$, $^{**}P < 0.01$, $^{*}P < 0.05$

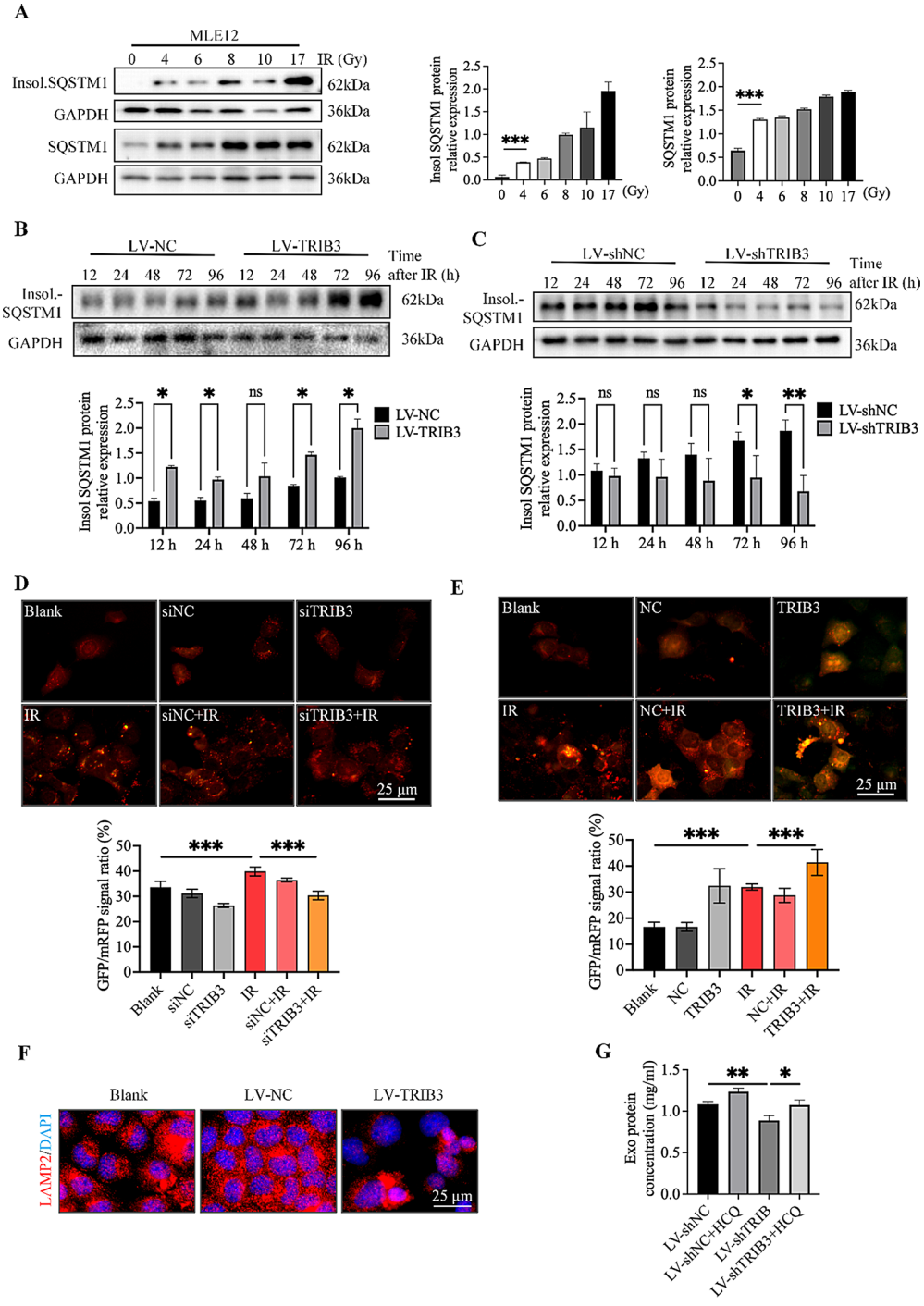

Fig. 7 TRIB3 inhibits autophagic flux to increase exosome secretion in MLE12. **(A)** Western blot and quantitative analysis of SQSTM1 and insoluble SQSTM1 protein in MLE12 cells. **(B)** Western blot and quantitative analysis of insoluble SQSTM1 protein after exposure of LV-TRIB3 MLE12 cells to 8 Gy irradiation for the indicated time. **(C)** Western blot and quantitative analysis of insoluble SQSTM1 protein after exposure of LV-shTRIB3 MLE12 cells to 8 Gy irradiation for the indicated time. **(D, E)** Representative fluorescent image and quantitative analysis of GFP/mRFP signal ratio to assess autophagic flux in MLE12 cells expressing mRFP-GFP-LC3 following TRIB3 silencing **(D)** or TRIB3 overexpression **(E). (F)** Representative immunofluorescence images of LV-NC and LV-TRIB3 MLE12 cells after exposure to 8 Gy irradiation, stained with LAMP2 (red) and DAPI (blue). (Bar = 25 μm). **(G)** Exosomes were isolated from the medium of irradiated LV-shTRIB3 MLE12 cells treated with hydroxychloroquine (HCQ) or not and quantified by BCA assays. Data represent exosome protein concentration distributions from three assays. All data are presented as mean ± S.E.M, ***$P < 0.001$, **$P < 0.01$, *$P < 0.05$

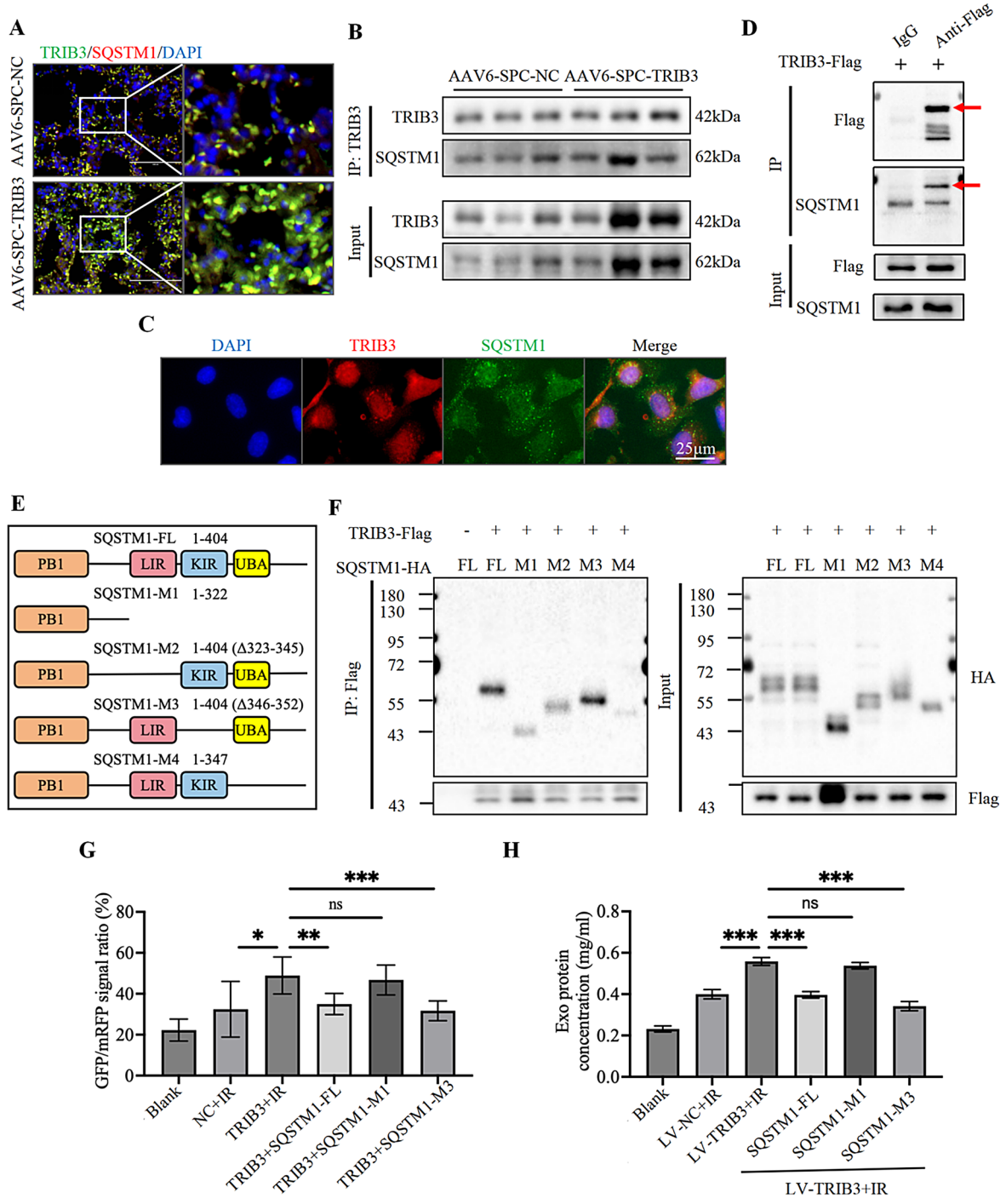

Fig. 8 TRIB3 interacts with SQSTM1. **(A)** Co-localization of TRIB3 (green) with SQSTM1 (red) in lung tissues of RIPF mice. (Bar = 200 μm). **(B)** Lung tissue extracts from RIPF mice were immunoprecipitated with anti-TRIB3 antibody and blotted with anti-SQSTM1 antibody. **(C)** Immunofluorescent staining showing the co-localization of TRIB3 (red) and SQSTM1 (green) in MLE12 cells transfected with TRIB3 plasmid. (Bar = 25 μm). **(D)** MLE12 cells were transfected with TRIB3-FLAG. Then, cell extracts were immunoprecipitated with anti-FLAG antibody. **(E)** A schematic representation of truncated mutations of SQSTM1. **(F)** MLE12 cells were co-transfected with indicated constructs of TRIB3-FLAG and SQSTM1-HA. Cell extracts were immunoprecipitated with anti-FLAG antibody and blotted with anti-HA antibody. **(G)** Quantitative analysis of GFP/mRFP signal ratio to assess autophagic flux in MLE12 cells expressing mRFP-GFP-LC3 following TRIB3 and SQSTM1co-overexpression. **(H)** Exosomes were isolated from the medium of irradiated LV-TRIB3 MLE12 cells following SQSTM1 overexpression and quantified by BCA assays. Data represent exosome protein concentration distributions from three assays. All data are presented as mean ± S.E.M, ***$P < 0.001$, **$P < 0.01$, *$P < 0.05$, ns: no significance

immunoprecipitation of TRIB3 from lung tissue extracts of RIPF mice demonstrated robust SQSTM1 co-precipitation (Fig. 8B). This interaction was also confirmed in MLE12 cells (Fig. 8C, D). Further analysis using several deletion mutants of HA-tagged SQSTM1 revealed that TRIB3 binds to the LIR and UBA domains of SQSTM1 (Fig. 8E, F), which are essential for LC3 and ubiquitinated protein binding [43]. Then We further investigated whether the interaction between TRIB3 and SQSTM1 influences autophagy flux and exosome secretion. Using MLE12 cells expressing the mRFP-GFP-LC3 reporter system, we demonstrated that co-overexpression of TRIB3 with either wild-type SQSTM1(SQSTM1-FL) or the KIR-truncated mutant (SQSTM1-M3) significantly rescued the impaired autophagy flux (as evidenced by reduced GFP/mRFP fluorescence ratio 48 h after 8 Gy irradiation) compared to TRIB3 overexpression alone, while the KIR + LIR + UBA-truncated mutant (SQSTM1-M1) showed no such restorative effect (Fig. 8G). The parallel experiments in LV-TRIB3 MLE12 cells revealed that overexpression of SQSTM1-FL or SQSTM1-M3 (but not SQSTM1-M1) similarly attenuated the radiation-induced exosome hypersecretion of TRIB3-overexpressing cells (Fig. 8H). These suggest that the LIR + UBA domains of SQSTM1 are necessary for both the autophagy blockade and exosome hypersecretion induced by TRIB3.

Thus, TRIB3 binds to SQSTM1, possibly disrupting its interaction with LC3 and ubiquitinated proteins in AEC II cell line MLE12, leading to SQSTM1 accumulation, autophagic dysfunction, and enhanced exosome secretion. Excessive exosome secretion promotes fibroblast proliferation and ECM production, accelerating RIPF progression.

Discussion

TRIB3 expression is upregulated under various stress conditions, including endoplasmic reticulum stress, starvation, oxidative stress, and hypoxia [13, 44]. Our study confirms that TRIB3 is also elevated in the lung tissues of RIPF mouse models. TRIB3 in AEC II cell line MLE12 inhibits autophagic flux by interacting with SQSTM1, enhances exosome secretion, and thus stimulates ECM production in fibroblasts. Knocking down TRIB3 in AEC II mitigates pathological changes associated with RIPF, whereas TRIB3 overexpression exacerbates these effects.

Autophagy is an evolutionarily conserved process critical for maintaining cellular homeostasis through the degradation of misfolded proteins and dysfunctional organelles, including peroxisomes and mitochondria [45]. Our findings demonstrated an accumulation of insoluble SQSTM1 in the RIPF mouse model, consistent with reduced autophagy observed in lung biopsies from patients with IPF [46, 47]. In irradiated MLE12 cells, we observed a blockage of autophagic flux, evidenced by the accumulation of insoluble SQSTM1 and confirmed through an mRFP-GFP-LC3 dual fluorescence assay, which indicated inhibited autophagic degradation.

The effects of irradiation on autophagy, however, remain controversial. For instance, studies by Madhuri et al. indicated that irradiation stimulates autophagy in macrophages, facilitating the clearance of misfolded proteins and damaged organelles and ultimately enhancing cell survival [10, 48]. Our study, by contrast, demonstrated that exposure of MLE12 cells to 8 Gy irradiation resulted in autophagic flux inhibition. Differences in cell types and radiation doses may account for these discrepancies.

TRIB3 has previously been shown to influence pathological processes by inhibiting autophagy, such as promoting glioblastoma proliferation [49], activating hepatic fibroblasts [50], and contributing to diabetes [51]. Our investigation extends these findings, demonstrating that TRIB3 impairs autophagy in AEC II during RIPF. Overexpression of TRIB3 in irradiated MLE12 cells led to SQSTM1 accumulation and a reduction in autophagic lysosomes, while TRIB3 knockdown restored autophagic flux. These in vitro findings were confirmed in animal models.

The mechanism by which TRIB3 inhibits autophagic flux in AEC II involves its interaction with SQSTM1. SQSTM1 is a receptor for ubiquitinated proteins destined for lysosomal degradation [52]. It binds to ubiquitinated proteins and LC3, incorporating them into autophagosomes for eventual lysosomal fusion and degradation. Our research shows that TRIB3 interacts with the LIR and UBA domains of SQSTM1, which are responsible for binding LC3 and ubiquitinated substrates, respectively, leading to SQSTM1 aggregation and impaired autophagic flux.

In other conditions, such as diabetes and liver fibrosis, TRIB3 similarly inhibits autophagic flux through interaction with SQSTM1, particularly via its UBA domain [17, 51]. In neurons, TRIB3 indirectly stimulates ULK1 by inhibiting its phosphorylation, promoting autophagosome formation while reducing autophagic flux [53]). In A549 and MiaPaCa-2 cells, TRIB3 interacts with Akt, reducing phosphorylation of Akt and its substrate PRAS40, thereby impairing autophagic flux through the Akt/mTORC1 pathway [54]. These findings highlight that TRIB3 modulates autophagy through different binding domains and pathways depending on cell type and tissue context.

Several studies have shown that autophagy regulation affects exosome biogenesis and release. For instance, autophagy induction in K562 cells through starvation or rapamycin treatment reduces exosome release by promoting fusion of autophagosomes with multivesicular bodies (MVBs) [55]. STX17, a protein involved in

autophagosome-lysosome fusion, also influences exosome production; its depletion increases exosome release in A549 cells [56]. Additionally, PIKfyve inhibition, which disrupts lysosome turnover, enhances exosome release and triggers secretory autophagy in PC-3 cells [57]. Our study supports these findings, showing that radiation-induced TRIB3 upregulation blocks autophagic flux, consequently increasing exosome release.

In healthy cells, most MVBs fuse with lysosomes, resulting in the degradation of their contents. Exosome secretion is restored when fusion of MVBs with lysosomes or autophagosomes is inhibited, indicating that lysosomal degradation primarily regulates exosome inhibition [58]. Furthermore, the ubiquitination status of MVB cargo proteins can influence MVB fate. While MVBs containing ubiquitinated MHC-II undergo lysosomal degradation in immature dendritic cells, non-ubiquitinated MHC-II is directed to the plasma membrane for secretion in activated dendritic cells [59]. Our findings suggest that TRIB3's interaction with the UBA domain of SQSTM1 may interfere with SQSTM1's role in transporting ubiquitinated proteins to MVBs, possibly leading to increased fusion of MVBs with the plasma membrane and heightened exosome release.

In the context of idiopathic pulmonary fibrosis (IPF), the disruption of the interaction between TRIB3 and GSK-3β has been shown to significantly mitigate pulmonary fibrosis [20]. Furthermore, TRIB3 is implicated in various oncological processes, notably in tumor immunity, stemness, drug resistance, and metabolic pathways. Peptide-based therapeutics targeting TRIB3 have demonstrated high specificity and considerable therapeutic potential in preclinical investigations [60]. These findings suggest that TRIB3 may serve as a promising therapeutic target. In the present study, we utilized a preventive intervention model to elucidate that TRIB3 influences the progression of RIPF through pre-radiation overexpression or knockdown in AEC II. Although our research has confirmed the pathogenic role of TRIB3 in RIPF development, future research using therapeutic intervention models where TRIB3 modulation is applied after radiation-induced lung injury will be essential to assess its viability as a druggable target for established RIPF.

While our study offers insights into the role of TRIB3 in the progression of RIPF, several limitations must be acknowledged. Although we demonstrated that exosomes derived from MLE12 cells influence extracellular matrix (ECM) production and the proliferation of lung fibroblasts, the specific exosomal cargoes contributing to RIPF progression remain unidentified. Comprehensive profiling of exosomal contents, such as RNA and proteins, will be a critical focus of our future investigations to elucidate these mechanisms. Furthermore, although the present study specifically examined the impact of TRIB3 on fibroblasts, it is essential to recognize that other key cellular components within the RIPF microenvironment, particularly immune cells like macrophages and T cells, play a crucial role in the pathogenesis and progression of RIPF [24, 61, 62]. Although MLE12 cells with features similar to AEC II, but are clearly very different from primary AEC II. To increase the robustness of our findings, future research should integrate a wider range of AEC II models, including both alternative immortalised cell lines such as RLE-6TN and primary AEC II cultures, to confirm the results presented in our manuscript.

Abbreviations

RIPF	Radiation-induced pulmonary fibrosis
AEC II	Alveolar epithelial type II cells
SASP	Senescence-associated secretory phenotype
SQSTM1/p62	Sequestosome 1
ECM	Extracellular matrix
IPF	Idiopathic pulmonary fibrosis
CF	Cystic fibrosis
ROS	Reactive oxygen species
NTA	Nanoparticle tracking analysis
AAV6	Adeno-associated virus serotype 6
HCQ	Hydroxychloroquine
LIR	LC3-interacting region
UBA	Ubiquitin-associated domain
GSVA	Gene set variation analysis
MVBs	Multivesicular bodies

Supplementary Information

The online version contains supplementary material available at https://doi.org/10.1186/s12931-025-03271-0.

Supplementary Material 1

Acknowledgements
Not applicable.

Author contributions
N.L. wrote the original manuscript, conducted experiments, and analyzed data; WY. Z. conducted experiments, analyzed data, and visualized the results; JL. L. interpretated the data; DF. Z., KJ. L., MM.Y. and XR. L. validated the results; LQ. D., C.X., and Q.L. contributed to the study conception and design; All authors read and approved the final manuscript.

Funding
This work was supported by the National Natural Science Foundation of China (32171239 and 82273580), Natural Science Foundation of Tianjin (23JCYBJC00490), CAMS Innovation Fund for Medical Science (2022-I2M-2-003).

Data availability
The RNA-seq data have been deposited at the NCBI SRA database with the accession number PRJNA1196531.

Declarations

Ethical approval
All animal experiments were approved by the Animal Ethical and Welfare Committee of the Institute of Radiation Medicine of Peking Union Medical College (IRM-DWLL-2021132).

Consent for publication
Not applicable.

Competing interests
The authors declare no competing interests.

Received: 8 February 2025 / Accepted: 8 May 2025
Published online: 21 May 2025

References

1. Chen Z, Wu Z, Ning W. Advances in molecular mechanisms and treatment of Radiation-Induced pulmonary fibrosis. Transl Oncol. 2019;12(1):162–9. https://doi.org/10.1016/j.tranon.2018.09.009.
2. Wang Y, Zhang J, Shao C. Cytological changes in radiation-induced lung injury. Life Sci. 2024;358:123188. https://doi.org/10.1016/j.lfs.2024.123188.
3. Debnath J, Gammoh N, Ryan KM. Autophagy and autophagy-related pathways in cancer. Nat Rev Mol Cell Biol. 2023;24(8):560–75. https://doi.org/10.1038/s41580-023-00585-z.
4. Guan R, Yuan L, Li J, Wang J, Li Z, Cai Z, Guo H, Fang Y, Lin R, Liu W, Wang L, Zheng Q, Xu J, Zhou Y, Qian J, Ding M, Luo J, Li Y, Yang K, Sun D, Yao H, He J, Lu W. Bone morphogenetic protein 4 inhibits pulmonary fibrosis by modulating cellular senescence and mitophagy in lung fibroblasts. Eur Respir J. 2022;60(6). https://doi.org/10.1183/13993003.02307-2021.
5. Luciani A, Villella VR, Esposito S, Brunetti-Pierri N, Medina D, Settembre C, Gavina M, Pulze L, Giardino I, Pettoello-Mantovani M, D'Apolito M, Guido S, Masliah E, Spencer B, Quaratino S, Raia V, Ballabio A, Maiuri L. Defective CFTR induces aggresome formation and lung inflammation in cystic fibrosis through ROS-mediated autophagy Inhibition. Nat Cell Biol. 2010;12(9):863–75. https://doi.org/10.1038/ncb2090.
6. Zhao X, Wei S, Li Z, Lin C, Zhu Z, Sun D, Bai R, Qian J, Gao X, Chen G, Xu Z. Autophagic flux blockage in alveolar epithelial cells is essential in silica nanoparticle-induced pulmonary fibrosis, Cell Death Dis 10(2) (2019) 127. http://doi.org/10.1038/s41419-019-1340-8.
7. Liu H, Fang S, Wang W, Cheng Y, Zhang Y, Liao H, Yao H, Chao J. Macrophage-derived MCPIP1 mediates silica-induced pulmonary fibrosis via autophagy. Part Fibre Toxicol. 2016;13(1):55. https://doi.org/10.1186/s12989-016-0167-z.
8. Zhao H, Wang Y, Qiu T, Liu W, Yao P. Autophagy, an important therapeutic target for pulmonary fibrosis diseases. Clin Chim Acta. 2020;502:139–47. https://doi.org/10.1016/j.cca.2019.12.016.
9. Turkkan G, Willems Y, Hendriks LEL, Mostard R, Conemans L, Gietema HA, Mitea C, Peeters S, De Ruysscher D. Idiopathic pulmonary fibrosis: current knowledge, future perspectives and its importance in radiation oncology. Radiother Oncol. 2021;155:269–77. https://doi.org/10.1016/j.radonc.2020.11.020.
10. Chaurasia M, Bhatt AN, Das A, Dwarakanath BS, Sharma K. Radiation-induced autophagy: mechanisms and consequences. Free Radic Res. 2016;50(3):273–90. https://doi.org/10.3109/10715762.2015.1129534.
11. Hill RM, Fok M, Grundy G, Parsons JL, Rocha S. The role of autophagy in hypoxia-induced radioresistance. Radiother Oncol. 2023;189:109951. https://doi.org/10.1016/j.radonc.2023.109951.
12. Hu L, Wang H, Huang L, Zhao Y, Wang J. Crosstalk between autophagy and intracellular radiation response (Review). Int J Oncol. 2016;49(6):2217–26. https://doi.org/10.3892/ijo.2016.3719.
13. Richmond L, Keeshan K. Pseudokinases: a tribble-edged sword. FEBS J. 2020;287(19):4170–82. https://doi.org/10.1111/febs.15096.
14. Ahn SH, Jang SK, Kim MJ, Kim G, Park KS, Hong J, Lee TG, Kim CH, Park IC, Jin HO. Downregulation of TRIB3 enhances the sensitivity of lung cancer cells to amino acid deprivation by suppressing AKT activation. Am J Cancer Res. 2024;14(4):1622–33. https://doi.org/10.62347/GLSY2976.
15. Chen L, Lin W, Zhang H, Geng S, Le Z, Wan F, Huang Q, Chen H, Liu X, Lu J J., Kong L. TRIB3 promotes malignancy of head and neck squamous cell carcinoma via inhibiting ferroptosis. Cell Death Dis. 2024;15(3):178. https://doi.org/10.1038/s41419-024-06472-5.
16. Li J, Zhang Q, Guan Y, Liao D, Chen H, Xiong H, Sheng Y, Chen X, Pang J. TRIB3 promotes the progression of renal cell carcinoma by upregulating the lipid droplet-associated protein PLIN2. Cell Death Dis. 2024;15(4):240. https://doi.org/10.1038/s41419-024-06627-4.
17. Zhang XW, Zhou JC, Peng D, Hua F, Li K, Yu JJ, Lv XX, Cui B, Liu SS, Yu JM, Wang F, Jin CC, Yang ZN, Zhao CX, Hou XY, Huang B, Hu ZW. Disrupting the TRIB3-SQSTM1 interaction reduces liver fibrosis by restoring autophagy and suppressing exosome-mediated HSC activation, Autophagy 16(5) (2020) 782–796. http://doi.org/10.1080/15548627.2019.1635383.
18. Saleem S, Biswas SC. Tribbles pseudokinase 3 induces both apoptosis and autophagy in Amyloid-beta-induced neuronal death. J Biol Chem. 2017;292(7):2571–85. https://doi.org/10.1074/jbc.M116.744730.
19. Lv X, Liu S, Liu C, Li Y, Zhang T, Qi J, Li K, Hua F, Cui B, Zhang X, Liu Y, Yu J, Yu J, Li L, Li X, Yao Z, Huang B. TRIB3 promotes pulmonary fibrosis through inhibiting SLUG degradation by physically interacting with MDM2. Acta Pharm Sin B. 2023;13(4):1631–47. https://doi.org/10.1016/j.apsb.2023.01.008.
20. Liu S, Lv X, Wei X, Liu C, Li Q, Min J, Hua F, Zhang X, Li K, Li P, Xiao Y, Hu Z, Cui B. TRIB3–GSK-3beta interaction promotes lung fibrosis and serves as a potential therapeutic target. Acta Pharm Sin B. 2021;11(10):3105–19. https://doi.org/10.1016/j.apsb.2021.06.017.
21. Wang L, Zhao W, Xia C, Li Z, Zhao W, Xu K, Wang N, Lian H, Rosas IO, Yu G. TRIB3 mediates fibroblast activation and fibrosis though interaction with ATF4 in IPF. Int J Mol Sci. 2022;23(24). https://doi.org/10.3390/ijms232415705.
22. Zheng D, Guo J, Liang Z, Jin Y, Ding Y, Liu J, Qi C, Shi K, Xie L, Zhu M, Wang L, Hu Z, Yang Z, Liu Q, Li X, Ning W, Gao J. Supramolecular nanofibers ameliorate Bleomycin-Induced pulmonary fibrosis by restoring autophagy. Adv Sci (Weinh). 2024;11(28):e2401327. https://doi.org/10.1002/advs.202401327.
23. Li LK, Wang N, Xu Y, Kaihua CJ, Ningnign H, Qin W, Yang L, Qiang L, Liqing D. Establishment and evaluation of radioactive pulmonary fibrosis model in SD rats, Int J Radiat Med Nucl Med 44(4) (2020) 52–58. http://doi.org/10.3760/cma.j.issn.1673-4114.2020.01.011.
24. Pan J, Li D, Xu Y, Zhang J, Wang Y, Chen M, Lin S, Huang L, Chung EJ, Citrin DE, Wang Y, Hauer-Jensen M, Zhou D, Meng A. Inhibition of Bcl-2/xl With ABT-263 Selectively Kills Senescent Type II Pneumocytes and Reverses Persistent Pulmonary Fibrosis Induced by Ionizing Radiation in Mice, Int J Radiat Oncol Biol Phys 99(2) (2017) 353–361. http://doi.org/10.1016/j.ijrobp.2017.02.216.
25. Love MI, Huber W, Anders S. Moderated estimation of fold change and dispersion for RNA-seq data with DESeq2, Genome Biol 15(12) (2014) 550. http://doi.org/10.1186/s13059-014-0550-8.
26. Ashburner M, Ball CA, Blake JA, Botstein D, Butler H, Cherry JM, Davis AP, Dolinski K, Dwight SS, Eppig JT, Harris MA, Hill DP, Issel-Tarver L, Kasarskis A, Lewis S, Matese JC, Richardson JE, Ringwald M, Rubin GM, Sherlock G. Gene ontology: tool for the unification of biology. The Gene Ontology Consortium, Nat Genet 25(1) (2000) 25– 9. http://doi.org/10.1038/75556.
27. Kanehisa M, Goto S. KEGG: kyoto encyclopedia of genes and genomes, Nucleic Acids Res 28(1) (2000) 27–30. http://doi.org/10.1093/nar/28.1.27.
28. Subramanian A, Tamayo P, Mootha VK, Mukherjee S, Ebert BL, Gillette MA, Paulovich A, Pomeroy SL, Golub TR, Lander ES, Mesirov JP. Gene set enrichment analysis: a knowledge-based approach for interpreting genome-wide expression profiles, Proc Natl Acad Sci U S A 102(43) (2005) 15545-50. http://doi.org/10.1073/pnas.0506580102.
29. review. Stem cell niche: structure and function. Annu Rev Cell Dev Biol (2017).
30. Saltykova IV, Elahi A, Pitale PM, Gorbatyuk OS, Athar M, Gorbatyuk MS. Tribbles homolog 3-mediated targeting the AKT/mTOR axis in mice with retinal degeneration, Cell Death Dis 12(7) (2021) 664. http://doi.org/10.1038/s41419-021-03944-w.
31. Lu YY, Fang YY, Wang SS, Guo J, Song JL, Zhu L, Lin ZK, Wang R, Zhang SY, Qiu WS, Qi WW. Cepharanthine sensitizes gastric cancer cells to chemotherapy by targeting TRIB3-FOXO3-FOXM1 axis to inhibit autophagy, Phytomedicine 135 (2024) 156161. http://doi.org/10.1016/j.phymed.2024.156161.
32. Colon-Cortes Y, Hasan MA, Aslanidi G. Intra-tracheal delivery of AAV6 vectors results in sustained transduction in murine lungs without genomic integration, Gene 763S (2020) 100037. http://doi.org/10.1016/j.gene.2020.100037.
33. Shen S, Wang P, Wu P, Huang P, Chi T, Xu W, Xi Y. CasRx-based Wnt activation promotes alveolar regeneration while ameliorating pulmonary fibrosis in a mouse model of lung injury, Mol Ther 32(11) (2024) 3974–3989. http://doi.org/10.1016/j.ymthe.2024.09.008.
34. Zent J, Guo LW. Signaling Mechanisms of Myofibroblastic Activation: Outside-in and Inside-Out, Cell Physiol Biochem 49(3) (2018) 848–868. http://doi.org/10.1159/000493217.
35. Klingberg F, Chau G, Walraven M, Boo S, Koehler A, Chow ML, Olsen AL, Im M, Lodyga M, Wells RG, White ES, Hinz B. The fibronectin ED-A domain enhances recruitment of latent TGF-beta-binding protein-1 to the fibroblast matrix, J Cell Sci 131(5) (2018). http://doi.org/10.1242/jcs.201293.
36. Chen L, Yang Y, Yue R, Peng X, Yu H, Huang X. Exosomes derived from hypoxia-induced alveolar epithelial cells stimulate interstitial pulmonary fibrosis through a HOTAIRM1-dependent mechanism, Lab Invest 102(9) (2022) 935–944. http://doi.org/10.1038/s41374-022-00782-y.
37. Colletti M, Ceglie D, Di Giannatale A, Nazio F. Autophagy and Exosomes Relationship in Cancer: Friends or Foes? Front Cell Dev Biol 8 (2020) 614178. http://doi.org/10.3389/fcell.2020.614178.

38. Lv X, Li K, Hu Z, Autophagy, Fibrosis P. Adv Exp Med Biol 1207 (2020) 569–579. http://doi.org/10.1007/978-981-15-4272-5_40.
39. Yue YL, Zhang MY, Liu JY, Fang LJ, Qu YQ. The role of autophagy in idiopathic pulmonary fibrosis: from mechanisms to therapies, Ther Adv Respir Dis 16 (2022) 17534666221140972. http://doi.org/10.1177/17534666221140972.
40. Yan XY, Zhong XR, Yu SH, Zhang LC, Liu YN, Zhang Y, Sun LK, Su J. p62 aggregates mediated Caspase 8 activation is responsible for progression of ovarian cancer, J Cell Mol Med 23(6) (2019) 4030–4042. http://doi.org/10.1111/jcmm.14288.
41. Zhang H, Ge S, Ni B, He K, Zhu P, Wu X, Shao Y. Augmenting ATG14 alleviates atherosclerosis and inhibits inflammation via promotion of autophagosome-lysosome fusion in macrophages, Autophagy 17(12) (2021) 4218–4230. http://doi.org/10.1080/15548627.2021.1909833.
42. Kimura S, Noda T, Yoshimori T. Dissection of the autophagosome maturation process by a novel reporter protein, tandem fluorescent-tagged LC3, Autophagy 3(5) (2007) 452–60.
43. Pankiv S, Clausen TH, Lamark T, Brech A, Bruun JA, Outzen H, Overvatn A, Bjorkoy G, Johansen T. p62/SQSTM1 binds directly to Atg8/LC3 to facilitate degradation of ubiquitinated protein aggregates by autophagy, J Biol Chem 282(33) (2007) 24131-45. http://doi.org/10.1074/jbc.M702824200.
44. Mondal D, Mathur A, Chandra PK. Tripping on TRIB3 at the junction of health, metabolic dysfunction and cancer, Biochimie 124 (2016) 34–52. http://doi.org/10.1016/j.biochi.2016.02.005.
45. Onorati AV, Dyczynski M, Ojha R, Amaravadi RK. Targeting autophagy in cancer, Cancer 124(16) (2018) 3307–3318. http://doi.org/10.1002/cncr.31335.
46. Tsoyi K, Liang X, De Rossi G, Ryter SW, Xiong K, Chu SG, Liu X, Ith B, Celada LJ, Romero F, Robertson MJ, Esposito AJ, Poli S, El-Chemaly S, Perrella MA, Shi Y, Whiteford J, Rosas IO. CD148 Deficiency in Fibroblasts Promotes the Development of Pulmonary Fibrosis, Am J Respir Crit Care Med 204(3) (2021) 312–325. http://doi.org/10.1164/rccm.202008-3100OC.
47. Araya J, Kojima J, Takasaka N, Ito S, Fujii S, Hara H, Yanagisawa H, Kobayashi K, Tsurushige C, Kawaishi M, Kamiya N, Hirano J, Odaka M, Morikawa T, Nishimura SL, Kawabata Y, Hano H, Nakayama K, Kuwano K. Insufficient autophagy in idiopathic pulmonary fibrosis, Am J Physiol Lung Cell Mol Physiol 304(1) (2013) L56-69. http://doi.org/10.1152/ajplung.00213.2012.
48. Chaurasia M, Gupta S, Das A, Dwarakanath BS, Simonsen A, Sharma K. Radiation induces EIF2AK3/PERK and ERN1/IRE1 mediated pro-survival autophagy, Autophagy 15(8) (2019) 1391–1406. http://doi.org/10.1080/15548627.2019.1582973.
49. Tang Z, Chen H, Zhong D, Wei W, Liu L, Duan Q, Han B, Li G. TRIB3 facilitates glioblastoma progression via restraining autophagy, Aging (Albany NY) 12(24) (2020) 25020–25034. http://doi.org/10.18632/aging.103969.
50. Ord T, Ord D, Ord T. TRIB3 limits FGF21 induction during in vitro and in vivo nutrient deficiencies by inhibiting C/EBP-ATF response elements in the Fgf21 promoter, Biochim Biophys Acta Gene Regul Mech 1861(3) (2018) 271–281. http://doi.org/10.1016/j.bbagrm.2018.01.014.
51. Hua F, Li K, Yu JJ, Lv XX, Yan J, Zhang XW, Sun W, Lin H, Shang S, Wang F, Cui B, Mu R, Huang B, Jiang JD, Hu ZW. TRB3 links insulin/IGF to tumour promotion by interacting with p62 and impeding autophagic/proteasomal degradations, Nat Commun 6 (2015) 7951. http://doi.org/10.1038/ncomms8951.
52. Katsuragi Y, Ichimura Y, Komatsu M. p62/SQSTM1 functions as a signaling hub and an autophagy adaptor, FEBS J 282(24) (2015) 4672-8. http://doi.org/10.1111/febs.13540.
53. Li K, Zhang TT, Hua F, Hu ZW. Metformin reduces TRIB3 expression and restores autophagy flux: an alternative antitumor action, Autophagy 14(7) (2018) 1278–1279. http://doi.org/10.1080/15548627.2018.1460022.
54. Erazo T, Lorente M, Lopez-Plana A, Munoz-Guardiola P, Fernandez-Nogueira P, Garcia-Martinez JA, Bragado P, Fuster G, Salazar M, Espadaler J, Hernandez-Losa J, Bayascas JR, Cortal M, Vidal L, Gascon P, Gomez-Ferreria M, Alfon J, Velasco G, Domenech C, Lizcano JM. The New Antitumor Drug ABTL0812 Inhibits the Akt/mTORC1 Axis by Upregulating Tribbles-3 Pseudokinase, Clin Cancer Res 22(10) (2016) 2508-19. http://doi.org/10.1158/1078-0432.CCR-15-1808.
55. Fader CM, Sanchez D, Furlan M, Colombo MI. Induction of autophagy promotes fusion of multivesicular bodies with autophagic vacuoles in k562 cells, Traffic 9(2) (2008) 230–50. http://doi.org/10.1111/j.1600-0854.2007.00677.x
56. Keller MD, Ching KL, Liang FX, Dhabaria A, Tam K, Ueberheide BM, Unutmaz D, Torres VJ, Cadwell K. Decoy exosomes provide protection against bacterial toxins, Nature 579(7798) (2020) 260–264. http://doi.org/10.1038/s41586-020-2066-6.
57. Hessvik NP, Overbye A, Brech A, Torgersen ML, Jakobsen IS, Sandvig K, Llorente A. PIKfyve inhibition increases exosome release and induces secretory autophagy, Cell Mol Life Sci 73(24) (2016) 4717–4737. http://doi.org/10.1007/s00018-016-2309-8.
58. Raudenska M, Balvan J, Masarik M. Crosstalk between autophagy inhibitors and endosome-related secretory pathways: a challenge for autophagy-based treatment of solid cancers, Mol Cancer 20(1) (2021) 140. http://doi.org/10.1186/s12943-021-01423-6.
59. Buschow SI, Nolte-'t Hoen EN, van Niel G, Pols MS, ten Broeke T, Lauwen M, Ossendorp F, Melief CJ, Raposo G, Wubbolts R, Wauben MH, Stoorvogel W. MHC II in dendritic cells is targeted to lysosomes or T cell-induced exosomes via distinct multivesicular body pathways, Traffic 10(10) (2009) 1528-42. http://doi.org/10.1111/j.1600-0854.2009.00963.x.
60. Lei S, Sun J, Xie Y, Xiao X, He X, Lin S, Zhang H, Huang Z, Wang H, Wu X, Peng H, Liu J. Diverse functions of Tribbles homolog 3 in cancers and its potential as a therapeutic target, Carcinogenesis 45(8) (2024) 527–542. http://doi.org/10.1093/carcin/bgae042.
61. Chen J, Wang C, Pan X, Zhan Y, Zhou W, Peng S, Chen C, Zhang M, Lan R, Wu J, Huang F, Hong J. Glycyrrhetinic Acid Mitigates Radiation-Induced Pulmonary Fibrosis via Inhibiting the Secretion of TGF-beta1 by Treg Cells, Int J Radiat Oncol Biol Phys 118(1) (2024) 218–230. http://doi.org/10.1016/j.ijrobp.2023.08.005.
62. Groves AM, Misra R, Clair G, Hernady E, Olson H, Orton D, Finkelstein J, Marples B, Johnston CJ. Influence of the irradiated pulmonary microenvironment on macrophage and T cell dynamics, Radiother Oncol 183 (2023) 109543. http://doi.org/10.1016/j.radonc.2023.109543.

Publisher's note